A High-Resolution Full-Earth Disk Model for Evaluating Synthetic Aperture Passive Microwave Observations From GEO

Boon H. Lim, *Member, IEEE*, and Christopher S. Ruf, *Fellow, IEEE*

***Abstract*—A proposed instrument for deployment on next-generation Geostationary Operational Environmental Satellite (GOES) platforms is the Geostationary Synthetic Thinned Aperture Radiometer (GeoSTAR). A high-resolution full-Earth disk model has been developed to aid in the design of the instrument and to characterize sensor performance. A number of ancillary geophysical data fields are used as inputs into a radiative-transfer model that also accounts for the propagation and viewing geometries from a geostationary Earth orbit (GEO). The model produces high-resolution (10 km $\times$ 10 km) simulated full-Earth disk microwave images from GEO. The model is used as a tool to examine several critical aspects of GeoSTAR performance and design. Differential image processing is assessed as a means of mitigating the effects of the Gibbs phenomenon; its performance is found to be excellent, even with nonideal *a priori* information. The spatial resolution and precision of images generated at 50 GHz are evaluated. The magnitude of the highest spatial-frequency components sampled by GeoSTAR is found to be well above its minimum detectable signal. However, the differential image processing removes most of the high-frequency content, which is due to static high-contrast boundaries in the scene. Most of the residual high-frequency content lies at or below the instrument noise floor.**

***Index Terms*—Microwave radiometry, remote sensing, synthetic aperture imaging.**

I. Introduction

GEOSTATIONARY Operational Environmental Satellite (GOES) platforms in geosynchronous Earth orbit (GEO) to date have not included microwave sensors due to the technical difficulties associated with matching the spatial-resolution performance of existing low-Earth-orbiting (LEO) sensors, such as the Advanced Microwave Sounding Unit (AMSU). Deployment in GEO would provide continuous temporal coverage and so is highly desirable. Achieving comparable spatial resolution to that in LEO with a traditional real aperture radiometer system would require a prohibitively large antenna, and difficulties arise in scanning the beam without platform disturbance. The difficulties can be overcome by a 2-D interferometric system. Interferometric imagers use highly thinned arrays of very small antennas to eliminate the need for a single large antenna, and their beam is scanned in software, negating the need for mechanical aperture scanning [1], [2]. The Geostationary Synthetic Thinned Aperture Radiometer (GeoSTAR) is such a system that is currently under development [3], [4]. GeoSTAR directly measures the spatial-frequency components of the brightness temperature (T_B) distribution, which are referred to as visibilities. Each sample of the visibility function corresponds to the cross correlation between a particular pair of antennas in the array. The physical separation between the antenna pairs determines which sample is measured. The vector-valued distances between antenna pairs are referred to as the baselines.

Operating at 50 and 183 GHz, GeoSTAR will provide temperature and water vapor soundings at significantly higher temporal resolution than is currently available from LEO [3], [4]. The instrument is designed to provide nadir resolution of 50 km (50 GHz) and 25 km (183 GHz) with new images generated approximately every 15 min. The difference in resolution results from differences in physical aperture size at the two frequencies. A highly resolved full-Earth disk model of the GeoSTAR brightness temperature image can be of great use in assessing the relationship between numerous instrument design parameters and the quality of the T_B images. Reduced spatial-scale Earth models have been successfully used to examine array distortion errors [5]. While appropriate for antenna redundancy and perturbation analysis, these models do not accurately account for the high-spatial-frequency components of the visibility measurement. Additional analyses have been performed, which compare GeoSTAR to a traditional scanning radiometer. They have the necessary spatial resolution ($\sim$5 km) but focus only on regional areas [6]. To this end, a high-resolution full-Earth disk model has been developed. It includes random noise levels expected of the actual instrument, but other nonideal characteristics of the hardware are not modeled. The spatial resolution of the model is 10 km in order to provide multiple samples within each pixel of both the coarser 50-GHz channels and the finer 183-GHz channels. For this analysis, only the 50-GHz channel is modeled.

The model would be beneficial to similar microwave instruments being developed internationally, including the Geostationary Atmospheric Sounder [7] in Sweden and the clock scanning interferometric radiometer [8] in China.

Manuscript received October 12, 2008; revised April 27, 2009 and August 4, 2009. First published October 9, 2009; current version published October 28, 2009. This work was supported in part by NASA Headquarters under the NASA Earth and Space Science Fellowship Program through Grant NNG05GP47H.

B. H. Lim is with the Instrument Systems Implementation & Concepts Section, NASA Jet Propulsion Laboratory, Pasadena, CA 91109 USA (e-mail: boon.h.lim@jpl.nasa.gov).

C. S. Ruf is with the Department of Atmospheric, Oceanic and Space Sciences, College of Engineering, University of Michigan, Ann Arbor, MI 48109-2143 USA (e-mail: cruf@umich.edu).

Color versions of one or more of the figures in this paper are available online at http://ieeexplore.ieee.org.

Digital Object Identifier 10.1109/TGRS.2009.2031172

0196-2892/$26.00 © 2009 IEEE

Authorized licensed use limited to: University of Michigan Library. Downloaded on October 30, 2009 at 15:29 from IEEE Xplore. Restrictions apply.

II. Full-Earth Disk Model Assumption

The inputs to the model are provided by a number of existing geophysical parameter models. In order to justify the use of these products, several key assumptions are made.

A. High-Frequency-Visibility Contributors

One key assumption in the generation of this model is that not all atmospheric parameters vary significantly at the highest resolved spatial scales of the GeoSTAR measurements. Most parameters are assumed to vary smoothly and, hence, to contribute only minimally to the high-frequency components of visibility. The major contributors to high-frequency visibilities are assumed to be the sharp transitions, particularly the following:

1) Earth disk/cosmic background;
2) continental boundaries;
3) clouds.

Of these three, only clouds change on the time scales of the measurement. While high-spatial-resolution measurements for all these three contributors are necessary, only the cloud parameters need to be updated regularly. It is this assumption that allows us to combine the appropriate data sets to produce the full-resolution inputs into the radiative-transfer model.

B. Scattering-Free Assumption at 50 GHz

The current model does not include scattering from precipitation—liquid or ice. The effects of liquid scattering are known to be minimal at 50 GHz since absorption effects dominate, except for large hydrometeors in stratiform and convective precipitation cells [9]. However, ice scattering aloft, particularly in deep convective storm cells, is known to reduce brightness temperatures, and these effects are also unaccounted for in the present model [10]. Scattering should be integrated into the model in order to extend its operation up to the 183-GHz channels of GeoSTAR, in general, and in order to improve the accuracy of the model at 50 GHz near deep convective systems.

III. Geophysical Parameter Model Data Sets

Some data sets used by the model are obtained from current spacecraft measurements. Other parameters are generated by numerical weather prediction (NWP) models. All of the chosen data sets are publicly distributed and available for access.

A. Surface Parameters and Vertical Atmospheric Profiles

The basis of the underlying atmosphere model is the National Centers for Environmental Prediction (NCEP) Global Data Assimilation System (GDAS). GDAS is generated every 6 h using a medium-range forecast model and consists of the minimum set that is necessary to regenerate NCEP analysis fields. The primary benefit of using GDAS over other NCEP products is the spatial resolution of the GDAS1 data set at $1.0^\circ \times 1.0^\circ$ gridded equally over the globe (1° in latitude at nadir is approximately 100 km). The data are reported at 26 vertical levels for temperature and geopotential height and 21 levels for relative humidity. In addition to the vertical profiles, GDAS also provides surface fields, including wind speed, which is necessary for the generation of the ocean-emissivity product.

B. Land-Surface Emissivity

Land-surface emissivity is derived from land-use classification maps. However, the emissivity will vary, depending on the conditions at any given location, particularly due to varying moisture content, which is not easily available. The French "Groupe de Modélisation pour l'Assimilation et la Prévision" (GMAP) provides land emissivity atlases that are derived from cloud-free measurements made using various satellite microwave radiometers (Special Sensor Microwave/Imager, Tropical Rainfall Measuring Mission Microwave Imager, and AMSU). We rely primarily on the product derived from AMSU [11]. Emissivity values derived from the measurements are binned into low and high incidence angles, and atlases are available in the form of monthly averages. The difference in the mean emissivity between the two incidence angle bins is found to be 0.023 at 50.3 GHz [12], and for all frequencies, emissivity is larger at lower incidence angles.

C. SSS

Ocean-emissivity calculations require sea-surface-salinity (SSS) values. The World Ocean Atlas from the Ocean Climate Laboratory provides objective analyses and statistics for various parameters, including ocean temperature, salinity, and dissolved oxygen. These fields are available on a $1.0^\circ \times 1.0^\circ$ grid and are generated roughly every four years. The most recent version was produced in 2005 [13]. The chosen data set is the objectively analyzed monthly means that are smoothed filled fields. While the salinity field is a necessary input for generating the ocean emissivity, it has only a secondary effect on emissivity at GeoSTAR frequencies. The single parameter with the largest bearing on the emissivity value is the incidence angle.

D. Cloud Products

A high-resolution cloud product is integral to the development of the full-Earth model. Products derived from GOES data are used. The NASA Langley Cloud and Radiation Research Group generates a cloud product utilizing an algorithm that combines the visible infrared solar-infrared split-window technique, solar-infrared infrared split-window technique, and solar-infrared infrared near-infrared technique [14]. Additional inputs to the algorithm include temperature and humidity profiles from NOAA Rapid Update Cycle or Global Forecast System forecasts to provide estimates of skin temperature, cloud height, and radiance attenuation calculations. Surface-type definition is based on the International Geosphere–Biosphere Program surface map, spatial distributions of snow/ice are taken from real-time maps generated by the NOAA/NESDIS Interactive Multisensor Snow and Ice Mapping System, and clear-sky reflectance data from the Clouds and the Earth's Radiant Energy System are used to provide background radiances for cloud detection and retrieval [15].

Authorized licensed use limited to: University of Michigan Library. Downloaded on October 30, 2009 at 15:29 from IEEE Xplore. Restrictions apply.

TABLE I
SUMMARY OF THE VARIOUS GEOPHYSICAL PARAMETER DATA SETS USED

Measured Parameters	Data Source	Spatial Res.	Temporal Res.	Levels
Land Emissivity	NWPG France	50km x 50km	Monthly Averages	Surface
Ocean Wind Speed	NCEP GDAS	100km x 100km	6 Hour Refresh	Surface
Sea Surface Temp.	NCEP GDAS	100km x 100km	6 Hour Refresh	Surface
Sea Surface Salinity	WOA 2005	100km x 100km	Monthly Averages	Surface
Temperature Profile	NCEP GDAS	100km x 100km	6 Hour Refresh	26 Pressure Levels
Geopotential Height	NCEP GDAS	100km x 100km	6 Hour Refresh	26 Pressure Levels
Humidity Profile	NCEP GDAS	100km x 100km	6 Hour Refresh	22 Pressure Levels
Surface Parameters	NCEP GDAS	100km x 100km	6 Hour Refresh	Surface
Cloud Liquid/Ice water	NASA LaRC	8km x 8km	~3 Hour Refresh	
Cloud Top/Bottom Temp.	NASA LaRC	8km x 8km	~3 Hour Refresh	
Land Sea Mask	GODAE GHSTT	1km x 1km	Generated in 2002	Surface
Digital Elevation Map	NGDC	4km x 4km	Generated in 2006	Surface

These products are generated by the NASA Langley Cloud and Radiation Research Group in near real time to support NWP models (validation and assimilation), estimating surface atmospheric radiation budgets and other "nowcasting" applications. The most recent release of the data set extends the Continental United States to a full GOES-East disk.

E. Land/Sea Mask

The land/sea mask is crucial for the determination of transitions between the widely differing surface-emissivity values between land and ocean. These sharp transitions have a significant impact on the magnitude of visibilities. The GODAE High Resolution Sea Surface Temperature Pilot Project land/sea mask is used [16]. The 1 km $\times$ 1 km resolution product is derived from a similar product available from the United States Geological Survey and covers latitudes 80.3° N to 80.3° S and all longitudes. The reduced latitude range is compatible with GEO modeling requirements.

The resolution of the land/sea mask is an order of magnitude finer than our needs. The effective emissivity of each 10 km $\times$ 10 km surface pixel in the radiative-transfer model is generated using an area-weighted average of the emissivity of each 1 km $\times$ 1 km pixel. This processing reduces the introduction of unrealistic high-frequency-visibility components.

F. DEM

A digital elevation map (DEM) provides the surface height, above which atmospheric profiles are integrated for the radiative-transfer calculation. The National Geophysical Data Center ETOPO2v2 Global Gridded 2-min Database is used [17]. Its vertical resolution is 1 m, and the horizontal resolution is approximately 4 km $\times$ 4 km. The values from the 4 km $\times$ 4 km grid are interpolated to the 10 km $\times$ 10 km grid.

G. Summary

Table I summarizes the various data sets that are used as inputs to the model, noting in particular their temporal and spatial resolutions. The highlighted values represent those data sets with spatial resolution of 8 km or better. A total of six different data sets are utilized to produce the high-resolution Earth disk model.

IV. GEOPHYSICAL PARAMETER MODELS

In addition to the raw input data, many other variables have to be derived utilizing the appropriate geophysical parameter model prior to the application of the radiative-transfer model. The following summarizes the various models used.

A. Ocean Emissivity

The dielectric constant of water is computed from the Klein–Swift model [18]. A correction for roughness and foam fraction is calculated using coefficients from FASTEM-2 developed for Radiative Transfer for the TIROS Operational Vertical Sounder (TOVS) (RTTOV), with algorithms and software developed for TOVS [19]. The specific coefficients used are those optimized for AMSU-A, the Polar Operating Environmental Satellite version instrument that performs GeoSTAR-like measurements. Inputs to the model include frequency, temperature, salinity, wind speed, and the angle of incidence of the measurement. The model produces as outputs the ocean-surface emissivity at both vertical and horizontal polarizations.

B. Gaseous Absorption

Absorption for both atmospheric gases and gaseous water vapor is calculated using the Rosenkranz absorption model Rosenkranz [20]. The model provides absorption coefficients for oxygen, nitrogen, and water vapor for the given frequency, temperature, pressure, and water vapor density.

C. Cloud Parameters

Cloud-liquid absorption is calculated under the assumption that the absorption is proportional to the column density of the cloud liquid [21]. Cloud-liquid profiles are assumed to be uniform up to the freezing level and to integrate up to a specified cloud-liquid path. This approximation is valid to the first order because no distinction is made among different cloud types. As such, applying any specific profile to the entire Earth disk would not improve the accuracy. The vertical profile of liquid in the freezing layer is assumed to decay exponentially [22].

Authorized licensed use limited to: University of Michigan Library. Downloaded on October 30, 2009 at 15:29 from IEEE Xplore. Restrictions apply.

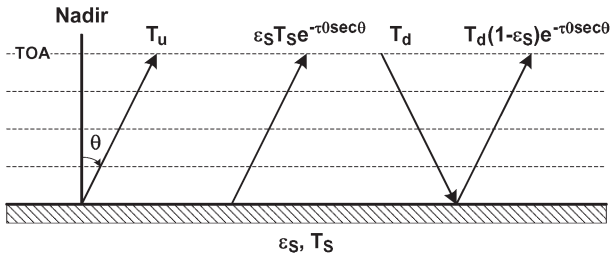


Fig. 1. Diagram showing the components of radiative-transfer calculation.

V. Radiative-Transfer Model and Coordinate System

A. Radiative-Transfer Model

Scattering-free radiative transfer is used to calculate the top-of-atmosphere brightness temperature [9]. Fig. 1 shows the individual components that are calculated.

B. Geophysical Parameter Grid

The 10 km × 10 km geophysical parameter grid has variable longitude spacing that is dependent on latitude. The longitude spacing increases to compensate for the decreasing circumference of the latitude circle as the coordinates approach either pole. The resulting geophysical parameter grid has pixels that are equal in area. While the atmosphere is assumed to be plane parallel, each pixel in each layer is based on the actual atmospheric state, so that the atmosphere is not homogeneous across each layer.

C. GeoSTAR Image Grid

The GeoSTAR image grid is oversampled and equally spaced in units of direction cosine. The nadir pixel size on the Earth disk is 10 km and increases off nadir. The proposed Y-array design, consisting of $N = 100$ array elements per arm with an arm length $R = 2.24$ m at a frequency of $f = 50$ GHz, results in a nadir pixel size of 50 km. Points on the GeoSTAR grid are selected and colocated on the geophysical parameter grid in terms of latitude and longitude, and the direction of propagation of radiation is determined by the GEO geometry. The radiative-transfer model is then applied at these points. The positions of the pixels on the Earth disk are calculated using the vertical plane of projection [23].

VI. Image Polarization

The polarization in the image plane is determined independently for each pixel. The current GeoSTAR design uses linearly polarized antennas. However, the emission from the polar region is orthogonal to that at the equatorial limb and varies across the entire Earth disk, except at nadir. The emissivity values of the GMAP surface atlases and those derived from the ocean-emissivity model are combined to generate a full-Earth emissivity map. Polarization is defined at the North Pole and rotated accordingly across the Earth disk. Fig. 2 shows the resulting combined vertical-polarization emissivity map.

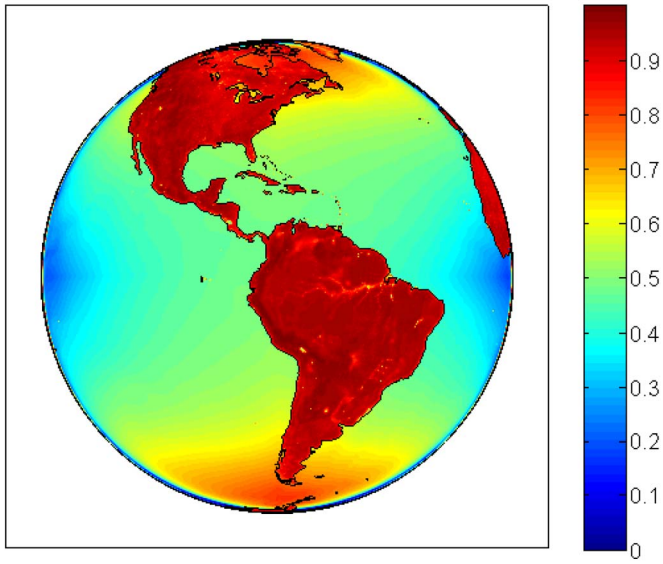


Fig. 2. Combined emissivity map with vertical polarization at the poles (August 2008).

VII. Instrument Simulator

The GeoSTAR simulator utilizes a rectangular sampling scheme in both spatial and visibility domains. The actual flight design uses a thinned Y-array of antenna elements, which results in hexagonal sampling in the visibility domain. While algorithms exist to utilize rectangular functions to produce hexagonal outputs [24], [25], the rectangular processing is used for simplicity. For the purposes of the analyses and conclusions presented here, the use of rectangular processing is considered adequate. Our analyses and conclusions are based on the expected range of values of visibilities over different portions of the spatial-frequency spectrum, not on their exact values at specific spatial frequencies. These ranges are not affected by whether the spectrum is sampled by a rectangular or hexagonal grid, specifically at the larger baselines that are of particular interest.

A. NEΔV

The noise-equivalent delta visibility (NEΔV)—a term similar to the noise-equivalent delta temperature (NEΔT) defined for a real-aperture radiometer system—characterizes the sensitivity of the visibility measurement. NEΔV refers to the additive zero-mean Gaussian noise that is present in each measurement of visibility. The standard deviation of that noise, $\sigma_{\mathrm{NE}\Delta\mathrm{V}}$, is given for the GeoSTAR system [4] by

$$\sigma_{\mathrm{NE}\Delta\mathrm{V}} = \frac{1}{\eta_q}\frac{T_s}{\sqrt{2B\tau}} \tag{1}$$

where η_q is the quantization efficiency, T_s is the system noise temperature, B is the predetection (intermediate-frequency) bandwidth, and τ is the integration time. The factor of two in (1) accounts for the decorrelation between noise originating from different channels of a correlating radiometer. The current GeoSTAR design for the temperature sounding channels utilizes 2-b correlations ($\eta_q = 0.88$) [26] and has an expected

Authorized licensed use limited to: University of Michigan Library. Downloaded on October 30, 2009 at 15:29 from IEEE Xplore. Restrictions apply.

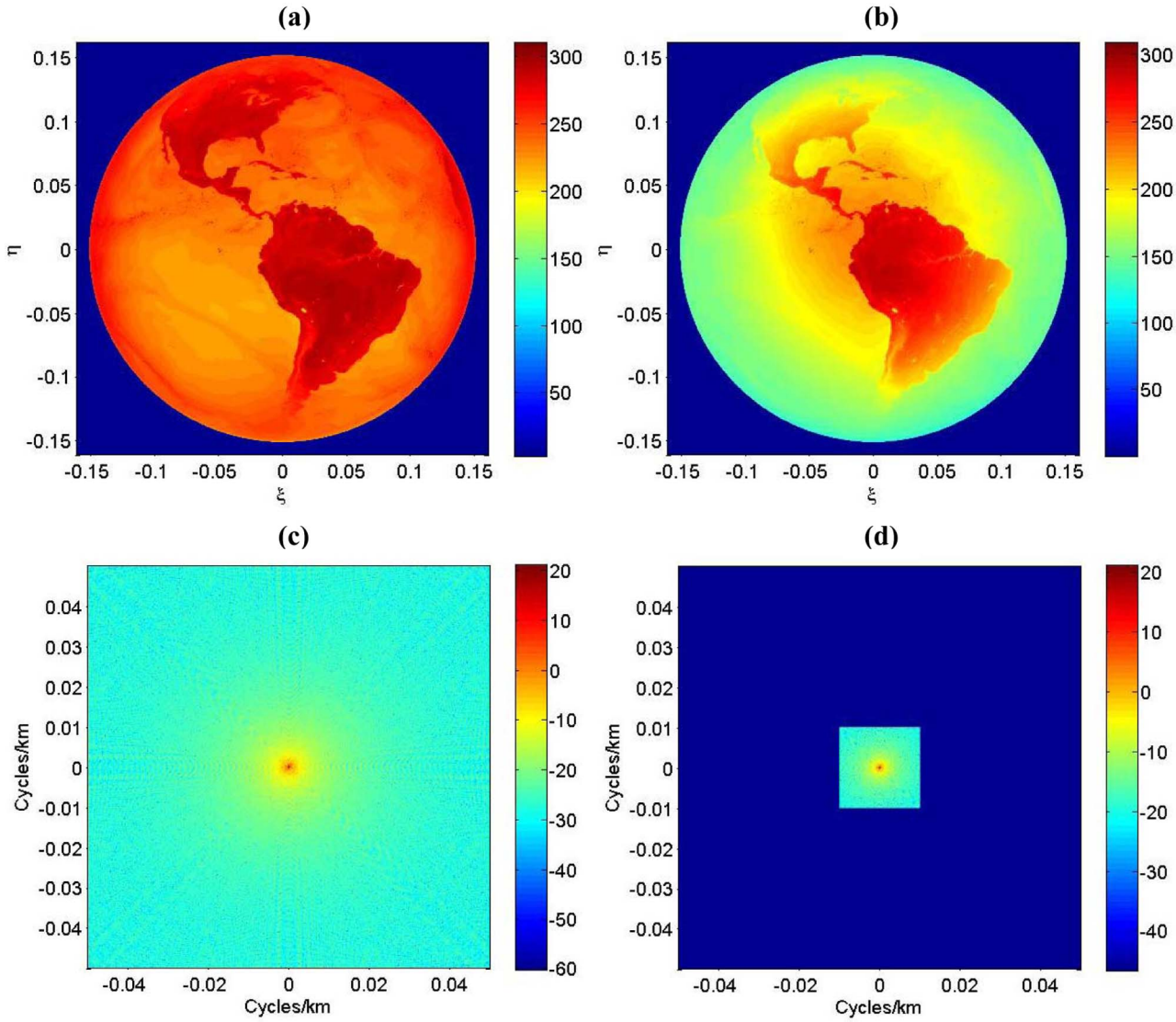


Fig. 3. Image of the intermediate products generated by the baseline algorithm. (a) Highest spatial resolution (10 km) T_B image (in kelvins). (b) T_B image with antenna taper applied (in kelvins). (c) Spatial-frequency components of an image after 2-D FFT application (in decibels). (d) Spatial-frequency components after truncation to a GeoSTAR spatial resolution of 50 km (in decibels). A resolution of 50 km follows from an antenna architecture of 100 elements per arm in a Y-array with 3.77λ interelement spacing.

system noise of $T_s = 400$ K (the expected receiver noise temperature is 250 K) and a predetection bandwidth of $B = 200$ MHz.

The additive noise that is present in the real and imaginary components of visibility is generally uncorrelated, so that the noise associated with measurements of the magnitude of the complex visibility will have a standard deviation given by

$$\sigma_{|V|} = \sqrt{\sigma^2_{\mathrm{NE}\Delta\mathrm{V_real}} + \sigma^2_{\mathrm{NE}\Delta\mathrm{V_imag}}} = \sqrt{2}\sigma_{\mathrm{NE}\Delta\mathrm{V}}. \quad (2)$$

B. Retrieved-Image Pixel Noise

The relationship between the noise in the raw visibility samples, NEΔV, and the per-pixel noise in the brightness temperature image is given by

$$\sigma_{T(\xi,\eta)} \approx W_A(\xi,\eta)\sqrt{2N\sigma^2_{\mathrm{NE}\Delta\mathrm{V}}} = W_A(\xi,\eta)\sqrt{N\sigma^2_{|V|}} \quad (3)$$

where $\sigma_{T(\xi,\eta)}$ is the standard deviation of the noise in the T_B image, (ξ,η) are the direction cosine coordinates, N is the total number of visibility samples needed to reconstruct the image, and W_A is a weighting due to the array-element antenna pattern. The weighting of the element antenna pattern is 1.7 at nadir and increases off nadir for traditional antenna patterns [27]. If we require a nadir pixel $\sigma_{T(0,0)}$ of 0.85 K and assume that $N = 60,600$ visibility measurements are required (resulting from 100 elements per arm) [4], the required $\sigma_{\mathrm{NE}\Delta\mathrm{V}}$ is 1.44 mK. If this value for $\sigma_{\mathrm{NE}\Delta\mathrm{V}}$ is inserted into (1), the corresponding integration time is $\tau = 250$ s. This is the minimum refresh time required to produce images of T_B with 0.85-K precision.

C. Baseline Processing Algorithm

The procedure followed to generate a simulated GeoSTAR T_B image accounts for the fact that measurements are made in

Authorized licensed use limited to: University of Michigan Library. Downloaded on October 30, 2009 at 15:29 from IEEE Xplore. Restrictions apply.

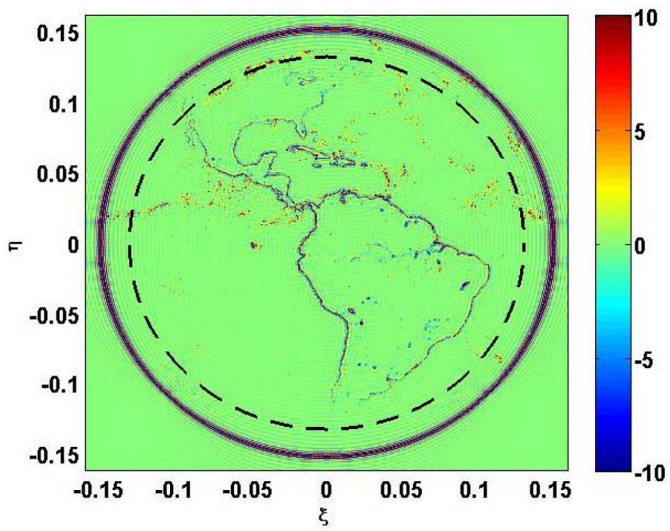


Fig. 4. ΔT_B image indicating the significant presence of Gibbs ringing (in kelvins). The dashed line shows the 60° incidence-angle boundary from a GEO sounder.

the spatial-frequency domain and that some information is lost due to the limited extent of the sampling. The procedure is as follows.

1) The T_B image is generated at the highest resolution possible (∼10 km).
2) An elemental antenna taper is applied to the image.
3) A rectangular 2-D Fourier transform is applied.
4) Fourier components are removed to match the GeoSTAR resolution (∼50 km).
5) NEΔV noise is added.
6) An apodization function (if any) is applied.
7) An inverse 2-D Fourier transform is applied.
8) An inverse elemental antenna taper is applied to the image.

The image produced as the output of the final step will be referred to as $\hat{T}_B$.

Fig. 3 shows examples of the outputs of each of the first four processing steps. The final result is the visibility product that GeoSTAR would measure. Comparing Fig. 3(c) and (d), the information lost to a GeoSTAR imager that is unable to image all spatial frequencies can be seen. For the nominal processing algorithm, the apodization applied will be uniform.

Fig. 4 shows an example of the difference between the GeoSTAR measurements and the original image, i.e., $\Delta T_B = \hat{T}_B - T_B$. The Gibbs artifacts at the step transitions at the continental boundaries and Earth disk transition are apparent.

VIII. Simulation Results

A. Comparison to an Ideal Real Aperture Antenna

An ideal uniformly illuminated circular aperture antenna has a 3-dB beam width defined by the following [28]:

$$\beta_{3\,\mathrm{dB}} = \frac{1}{2R_\lambda} \tag{4}$$

where R_λ is the aperture radius divided by the measurement wavelength. The equivalent expression for the 3-dB beam width for a Y-array is given by [29]

$$\beta_{3\,\mathrm{dB}}^{\mathrm{Hex}} = \frac{\pi}{2}\frac{1}{r_{\lambda,\max}2\sqrt{3}} \tag{5}$$

where $r_{\lambda,\max}$, the length of a single Y-array arm in wavelengths, is the effective radius of the synthesized GeoSTAR aperture. Equating (4) and (5), we arrive at the relationship between a circular aperture radius and the dimension that defines a synthetic aperture radiometer

$$R_\lambda = \frac{2\sqrt{3}}{\pi} r_{\lambda,\max} \approx 1.10\, r_{\lambda,\max}. \tag{6}$$

Thus, a real aperture antenna has dimensions that are ∼10% larger than that of a synthetic aperture radiometer with an equivalent 3-dB beam width. Note that the real-aperture-antenna pattern will have a first sidelobe level of ∼13 dB, whereas (5) assumes an ∼6.6-dB first sidelobe level for GeoSTAR.

Table II summarizes the parameters of interest for the real and synthetic aperture antennas to be compared. The real aperture antennas are sized such that the 3-dB beam widths of the equivalent synthetic aperture systems are equal. From the table, it can be seen that, with aperture synthesis, a smaller physical aperture can achieve the same angular resolution as a real aperture imager can, provided that a uniform aperture taper is used (resulting in alternating positive and negative sidelobes).

A comparison between GeoSTAR images generated with a uniform and a triangular taper was performed to assess the impact of having alternating positive and negative sidelobes (in the uniform case). The retrieved image from the synthetic aperture is generated assuming that the elemental antenna patterns are known and identical and follow the shape of the parabolic Potter horn [4]. The synthetic aperture with a taper has a triangular apodization applied, where the taper is a function of a single radial variable [30]. In addition, no noise is added to the images. The calculated errors represent the standard deviation of the difference image (the difference between the Earth model output and the instrument simulator output), evaluated across the full image, the image pixels on the Earth disk only, and the pixels extending to an Earth incidence angle of 60°. The 60° limit is consistent with the upper bound of where most current GOES products are deemed useful.

Tables III and IV summarize the results for two different days, with one day representing the start of the hurricane season and the other day being the time when Hurricane Gustav made landfall in Louisiana during fall 2008, approximately three months apart for only the synthetic aperture.

In all cases, the errors decrease as the image extent narrows because the errors are largest near the Earth limb. Both tables exhibit very similar results, suggesting that these results are relatively insensitive to daily weather patterns.

B. Mitigation of the Gibbs Phenomenon

Fig. 4 shows that the largest retrieval errors in an ideal synthetic array are from the known effects of the Gibbs phenomenon, where ringing artifacts occur in regions with sharp

Authorized licensed use limited to: University of Michigan Library. Downloaded on October 30, 2009 at 15:29 from IEEE Xplore. Restrictions apply.

TABLE II
ANTENNA PARAMETER COMPARISON AT 50.3 GHZ

Parameter	Real Aperture*		Synthetic Aperture	
β_{3dB} [deg]	0.09^0	0.07^0	0.07^0	0.09^0
Radius [m]	**1.83**	**2.48**	**2.24**	**2.24**
Radius [λ]	327	416	377	377
Aperture taper	Uniform	Uniform	Uniform	Triangular
First Side lobe level [dB]	13	13	6.7	13
Side lobe sign	Positive	Positive	Positive/Negative	Positive

* In practice, real aperture antennas would generally have an additional aperture taper applied to lower their side lobe levels. This would increase their size for a given beam width..

TABLE III
GEOSTAR IMAGE ERROR AT 50.3 GHZ: CASE 1—JUNE 2, 2008 18Z

Aperture Taper	Full Image [K]	Earth Disk [K]	Region ($<60^0$) [K]
Uniform	8.3	6.9	2.3
Triangular	9.6	7.7	2.6

TABLE IV
GEOSTAR IMAGE ERROR AT 50.3 GHZ:
CASE 2—SEPTEMBER 1, 2008 18Z

Aperture Taper	Full Image [K]	Earth Disk [K]	Region ($<60^0$) [K]
Uniform	8.3	6.9	2.2
Triangular	9.6	7.7	2.4

transitions. Mitigation of this phenomenon can be performed using differential analysis with respect to an *a priori* image. The mitigated image can be expressed as

$$\hat{T}_B = T_{B_\mathrm{Model}} + G'(V - GT_{B_\mathrm{Model}}) \tag{7}$$

where T_{B_Model} is an *a priori* image (possible sources are discussed subsequently), G is a linear operator that models the action of the instrument on the T_B distribution (commonly referred to as the G-matrix [31]), G' (the pseudoinverse operator for G) represents the image reconstruction algorithm, and V denotes the measured visibilities. For the purposes of this analysis, the G-matrix can be considered to be a 2-D fast Fourier transform (FFT) of the image, with the appropriate truncation of the spatial-frequency extent, and G' to be the corresponding inverse, FFT^{-1}.

A sample T_B image will be examined in detail to illustrate the proposed solution to the Gibbs phenomenon. The image is derived from data sets assembled during the U.S. landfall of Hurricane Gustav on September 1, 2008, at 18Z. Fig. 5 shows the visible image as captured by GOES-East, illustrating the various cyclonic formations. Fig. 6 shows the corresponding model output T_B image at 50.3 GHz, with the color bar being scaled to accentuate the features over ocean. Features with fine spatial scales can be seen in Fig. 6 at the 10-km resolution of the model output.

A suitable *a priori* atmospheric model to be applied utilizes the GDAS atmosphere without any inclusion of the cloud product (Sections III-D and IV-C) and is termed the matched GDAS atmosphere. This model properly accounts for the increased atmospheric path length and the variable incidence angles across the scene. Fig. 7 shows the outputs from the baseline processing algorithm (left) and the associated differential processing algorithm (right), utilizing a matched GDAS atmosphere.

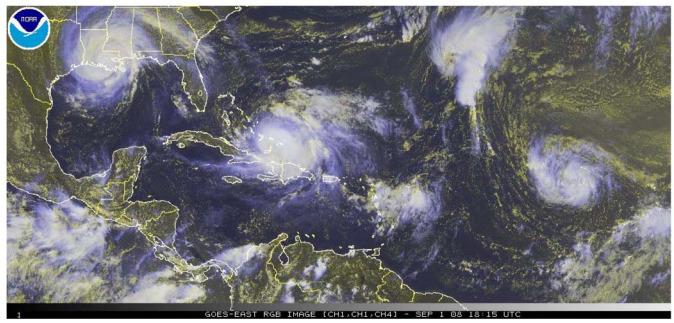


Fig. 5. Hurricane Gustav landfall with Hurricane Hanna over Haiti and Tropical Storm Ike in the Atlantic Ocean, GOES-E RGB image (September 1, 2008 18Z). Courtesy of NOAA's Satellite and Information Service.

By comparing the images in Fig. 7, it can be seen that the differential algorithm has reduced the Gibbs artifacts visually, particularly those due to nonatmospheric features such as land/sea boundaries.

A second differential algorithm is evaluated, in which the GDAS atmosphere that is used is mismatched, i.e., the prior atmosphere used is generated on a different day from the retrieval. In this case, the prior atmosphere chosen is at the same time of day but three months prior to the actual atmosphere to be retrieved. It includes different surface-emissivity maps for both the ocean and land, which are generated from the appropriate geophysical data sets (Sections III-B and C), surface parameters (Section III-A), and geophysical model (Section IV-A). As with the matched atmosphere, no cloud product is included in the mismatched atmosphere.

The impact of using a matched versus a mismatched atmosphere is presented in Table V, which lists the root-mean-square (rms) difference between the true and retrieved brightness temperatures for three cases: 1) if the differential algorithm is not used; 2) if the differential algorithm is used with a matched atmosphere (i.e., same-day temperature and humidity fields but clouds not matched); and 3) if the differential algorithm is used with a mismatched atmosphere (i.e., three-month prior atmosphere and no clouds). Almost all of the reduction in rms error due to the differential algorithm is present in both cases 2) and 3), suggesting that a large majority of the improvement provided by the differential algorithm is due to elimination of the ringing that is present at high-contrast land/ocean and Earth/space boundaries and not at lower contrast boundaries between cloudy and clear regions or due to changes in the air temperature and humidity distributions.

Authorized licensed use limited to: University of Michigan Library. Downloaded on October 30, 2009 at 15:29 from IEEE Xplore. Restrictions apply.

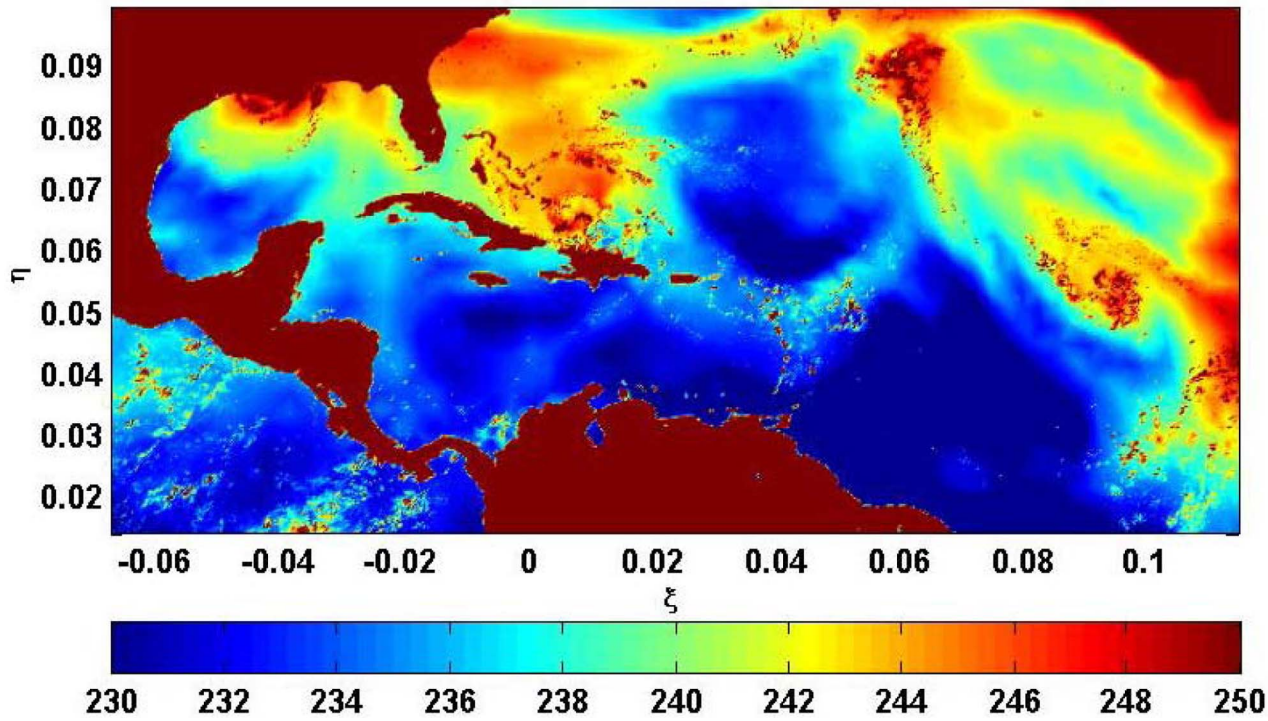


Fig. 6. Corresponding microwave version of Fig. 5, high-resolution model output (50.3 GHz, September 1, 2008 18Z) (in kelvins).

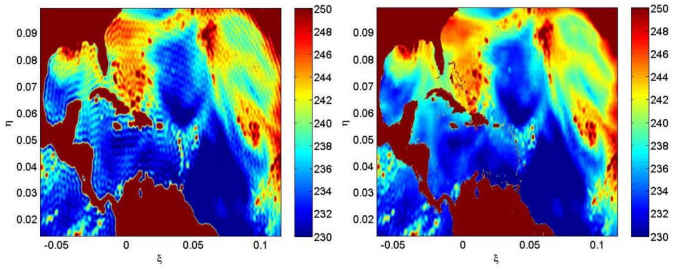


Fig. 7. High-resolution model output $\hat{T}_B$. (Left) Baseline processing. (Right) Differential processing with a matched GDAS atmosphere (50.3 GHz, September 1, 2008 18Z) (in kelvins).

While the results here are generated for a single scene, they are representative of the impact of differential processing in general. Even with an unmatched atmosphere, retrieval errors due to the Gibbs phenomenon can be reduced significantly.

Fig. 8 shows the difference images $(\Delta T_B = \hat{T}_B - T_{B_\mathrm{Model}})$ generated with a matched and a mismatched GDAS atmosphere with no additive noise and a uniform taper. Either of these images would be added to the prior image (T_{B_Model}) to form the actual reconstructed brightness temperature distribution. Note in both images that the strong ringing that is present near high-contrast boundaries in Fig. 7 (left) has been largely eliminated

Fig. 9 compares the differential processing of a matched atmosphere with and without noise added, focusing on the landfall region of Hurricane Gustav. Without noise, small Gibbs artifacts are still visible in the image from the discontinuities introduced by the Hurricane system. The addition of NEΔV noise masks the presence of the smaller Gibbs artifacts.

Mitigation of these smaller artifacts requires a more complex algorithm, for example, something similar to CLEAN [32] developed for radio astronomy. The suitability of CLEAN has been investigated in [33] with respect to instruments dealing with extended Earth sources, and a similar differential algorithm proposed using mean Earth disk temperatures. The closer the differential image is to quasi-point sources in an empty field, the more effectively a CLEAN-type algorithm performs. From Fig. 8, a CLEAN-type algorithm will perform better for the matched atmosphere than the mismatched one.

C. Spatial-Frequency Information Content

One of the key products of the high-resolution full-Earth disk model is a realistic model of the expected spatial-frequency content that is present at 50 GHz and of the visibilities that will be measured by a GeoSTAR-type instrument. Fig. 10 shows a scatter plot of the complex-visibility magnitudes that are expected at 50.3 GHz with respect to the absolute-baseline separation of an ideal imager $(\sqrt{u^2+v^2})$. The horizontal line shows the current recommended $\sigma_{|V|}$ level (2 mK) based on the requirements and indicates that, as the wavelength spacing increases, a larger portion of the visibilities fall below the instrument sensitivity. Figs. 10 and 11 are generated for one particular scene but are representative of any scene that GeoSTAR expects to measure. The highest spatial-frequency magnitudes can be expected to increase slightly with the addition of scattering to the radiative-transfer forward model.

In Fig. 10, the magnitude of visibilities generally decreases as the interferometer spacing increases. Because it is somewhat difficult to interpret the data in this form, the visibility space will be divided into annular rings, centered at the origin, in order to evaluate the antenna gain errors, in a similar manner as was used in [4]. The thresholds between annular regions are represented by the vertical lines in Fig. 10. The annular division

Authorized licensed use limited to: University of Michigan Library. Downloaded on October 30, 2009 at 15:29 from IEEE Xplore. Restrictions apply.

TABLE V
COMPARISON OF BRIGHTNESS TEMPERATURE RETRIEVAL ERRORS WITH VARIOUS PROCESSING ALGORITHMS (50.3 GHZ, SEPTEMBER 1, 2008 18Z)

Processing Method	Uniform Taper [K]			Triangular Taper [K]		
	Full Image	Earth Disk	$<60^0$	Full Image	Earth Disk	$<60^0$
1) No Differential Algo	8.3	6.9	2.3	10.7	8.5	2.7
2) Differential Algo with Matched Atmosphere	1.1	1.4	1.1	1.2	1.4	1.2
3) Differential Algo with Mismatched Atmosphere	1.2	1.4	1.2	1.3	1.5	1.3

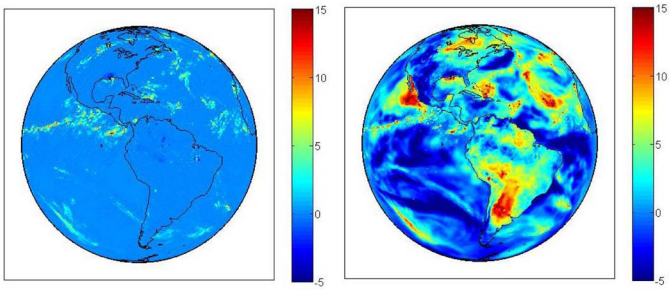


Fig. 8. ΔT_B using (left) a matched and (right) a mismatched GDAS atmosphere (50.3 GHz, September 1, 2008 18Z) (in kelvins).

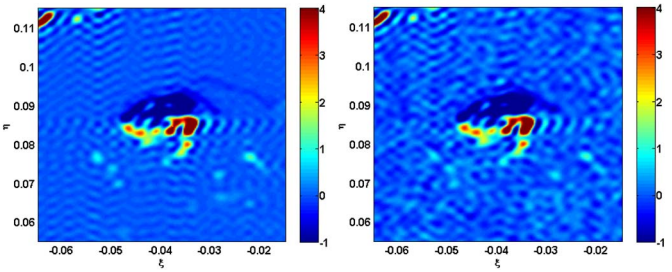


Fig. 9. ΔT_B of Hurricane Gustav landfall with a matched atmosphere, (left) assuming no noise and (right) adding the expected level of NEΔV noise to the measurements, which results in 0.85 K of rms noise in the T_B image (50.3 GHz, September 1, 2008 18Z) (in kelvins).

includes ten regions—one region for the "zeroth" visibility, eight annular regions in the circular band-limited area, and one region for all values outside of the circular band-limited area. The radii of the eight annular rings are roughly scaled in powers of two, where each area of coverage is three times the area of the enclosed area, except for the first and last regions. Both Figs. 10 and 11 show the visibility distribution of the eight annular regions within the circular band-limited area.

Fig. 11 shows the visibility distribution after the Gibbs mitigation algorithm with a matched atmosphere (as outlined in Section VIII-B) is applied. Without the contributions of high-contrast transitions, the magnitudes of visibilities decrease significantly such that a significant portion of the measured visibilities are now below the previously defined $\sigma_{|V|}$ level. The results are summarized in Table VI, where column 1 defines the various annular regions.

The rms of the complex-visibility magnitude is a measure of the signal strength of the measurements in each annular region, and the standard deviation gives an idea of the spread of these values. At 50.3 GHz, only the outermost annular region of the measured complex visibilities is within an order of magnitude of $\sigma_{|V|}$ with the nominal processing algorithm. However, for the matched-atmosphere Gibbs-mitigated scene, several of the

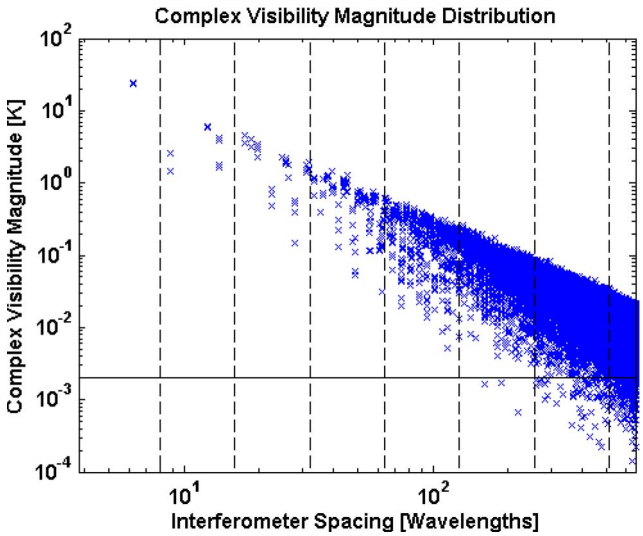


Fig. 10. Complex-visibility magnitude distribution (50.3 GHz, September 1, 2008 18Z) (in kelvins).

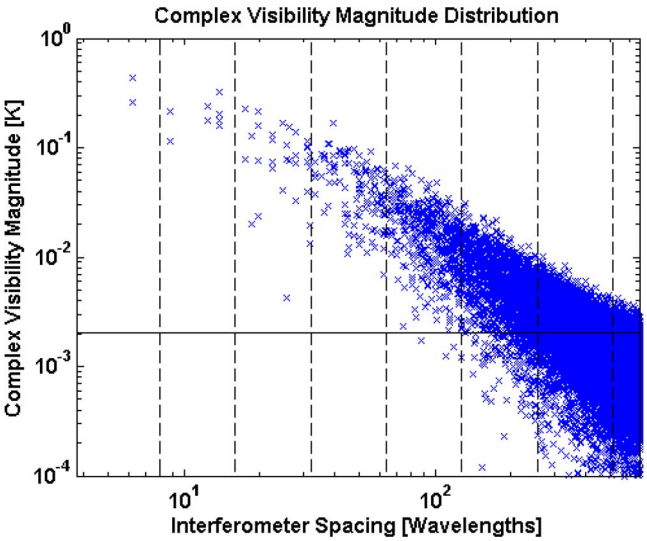


Fig. 11. Complex-visibility magnitude distribution, Gibbs mitigated, matched atmosphere (50.3 GHz, September 1, 2008 18Z) (in kelvins).

outer regions have rms magnitudes that are close to the noise level. The majority of high-spatial-frequency measurements are now indistinguishable from the inherent instrument noise.

The results clearly indicate that postprocessing strategies must be considered during the instrument design. Investigating perturbations in the atmospheric state will require a lower noise level; otherwise; the higher spatial frequencies will become redundant. Note that the matched-atmosphere Gibbs mitigation presents the worse case scenario with the most stringent noise requirements. The more likely state will be that of a mismatched

Authorized licensed use limited to: University of Michigan Library. Downloaded on October 30, 2009 at 15:29 from IEEE Xplore. Restrictions apply.

TABLE VI
VISIBILITIES DIVIDED INTO ANNULAR REGIONS (50.3 GHz, SEPTEMBER 1, 2008 18Z)

			Nominal Processing		Gibbs Mitigated	
Baseline Separation (λ)	Count (#)	Fraction (%)	RMS |V| (K)	STD |V| (K)	RMS |V| (K)	STD |V| (K)
0	1	0.002	78	-	0.078	-
> 0 to 8	4	0.008	24.0	0.32	0.028	0.0107
> 8 to 16	16	0.03	3.87	1.82	0.017	0.0054
> 16 to 32	68	0.013	2.14	1.07	0.013	0.0063
> 32 to 64	244	0.46	0.69	0.34	0.0080	0.0041
> 64 to 128	988	1.9	0.23	0.11	0.0046	0.0024
> 128 to 256	4088	7.5	0.082	0.042	0.0028	0.0014
> 256 to 512	15992	30.0	0.028	0.014	0.0014	0.0007
> 512 – 652	13232	24.8	0.014	0.006	0.0010	0.0005
> 652 - Max	18808	35.2	0.010	0.004	0.0008	0.0004

TABLE VII
RSS OF VISIBILITIES, HURRICANE GUSTAV LANDFALL (SEPTEMBER 1, 2008 18Z)

Baseline Separation (λ)	Count (#)	Fraction (%)	RSS V (K) 50.3 GHz	RSS V (K) 52.8 GHz	RSS V (K) 55.5 GHz
0	1	0.002	77.9	82.0	71.1
> 0 to 8	4	0.008	48.0	51.4	43.8
> 8 to 16	16	0.03	15.5	16.7	14.3
> 16 to 32	68	0.013	17.7	16.9	14.9
> 32 to 64	244	0.46	10.7	9.7	8.8
> 64 to 128	988	1.9	7.2	6.5	6.1
> 128 to 256	4088	7.5	5.3	4.8	4.5
> 256 to 512	15992	30.0	3.6	3.3	3.2
> 512 – 652	13232	24.8	1.6	1.5	1.5
> 652 - Max	18808	35.2	1.3	1.2	1.2

atmosphere, which would result in intermediate values between the nominal processing and Gibbs-mitigated values presented in Table VI.

As a means to evaluate the necessity of performing measurements at these larger baselines, the root sum square (RSS) of the visibility magnitude is calculated $(\mathrm{RSS} = \mathrm{rms} * \sqrt{\mathrm{Count}})$ to show the contribution of each visibility band to the retrieved image [4]. The results in Table VII suggest that, even at the outermost annular region, there still exists over 1.5 K of variability to be measured compared to channels moving up the wing of the oxygen line. This contribution is an order of magnitude larger than the corresponding noise contribution (0.27 K).

IX. CONCLUSION

A high-resolution full-Earth disk model has been created, which generates top-of-atmosphere 50-GHz T_B images, as seen from a GOES-East location. The model utilizes existing data sets to provide realistic inputs of the nonscattering atmospheric state and can be generated with varying initialization states (no winds, no clouds, etc.). Visibilities have been generated using an ideal 2-D FFT in rectangular coordinates to determine the expected distribution in the visibility domain. For evaluation of the statistics of visibilities associated with the large-baseline separation, the results will be similar to that of hexagonal processing.

Mitigation of the error in synthetic aperture images due to the Gibbs phenomenon has been demonstrated using a differential imaging technique that allows for sharp transitions to be filled in by *a priori* information. This method reduces the error significantly throughout the retrieved image and performs well, even when the atmospheric state is not matched and the *a priori* atmosphere is generated from data three months prior. Gibbs artifacts will still be produced from atmospheric events but with a much smaller magnitude. The remaining artifacts require a more complex algorithm for removal, which has been investigated in radio astronomy [32].

Evaluation of the information content in the spatial-frequency domain with realistic images has demonstrated that the contribution to the retrieved image decreases with increasing baseline separation. For the 50-GHz channels, there is over 2 K of variation in T_B contributed by spatial frequencies that lie outside of the circular band-limited area of measurements. The instrument sensitivity is dependent upon the integration time, and with the current design, the magnitudes of the measured complex visibilities are well above the instrument noise floor with nominal processing. However, with the proposed Gibbs mitigation strategy, the overall magnitude level of visibilities is decreased significantly, particularly for a well-matched atmosphere. The future GeoSTAR system should consider this impact during the design.

REFERENCES

[1] C. S. Ruf, C. T. Swift, A. B. Tanner, and D. M. Le Vine, "Interferometric synthetic aperture microwave radiometry for the remote sensing of the Earth," *IEEE Trans. Geosci. Remote Sens.*, vol. 26, no. 5, pp. 597–611, Sep. 1988.

[2] I. Corbella, N. Duffo, M. Vall-llossera, A. Camps, and F. Torres, "The visibility function in interferometric aperture synthesis radiometry," *IEEE Trans. Geosci. Remote Sens.*, vol. 42, no. 8, pp. 1677–1682, Aug. 2004.

[3] B. Lambrigtsen, W. Wilson, A. Tanner, T. Gaier, C. Ruf, and J. Piepmeier, "GeoSTAR—A microwave sounder for geostationary satellites," in *Proc. IGARSS*, Anchorage, AK, 2004, pp. 777–780.

Authorized licensed use limited to: University of Michigan Library. Downloaded on October 30, 2009 at 15:29 from IEEE Xplore. Restrictions apply.

[4] A. B. Tanner, W. J. Wilson, B. H. Lambrigtsen, S. J. Dinardo, S. T. Brown, P. P. Kangaslahti, T. C. Gaier, C. S. Ruf, S. M. Gross, B. H. Lim, S. Musko, S. Rogacki, and J. R. Piepmeier, "Initial results of the Geostationary Synthetic Thinned Array Radiometer (GeoSTAR) demonstrator instrument," *IEEE Trans. Geosci. Remote Sens.*, vol. 45, no. 7, pp. 1947–1957, Jul. 2007.

[5] F. Torres, A. B. Tanner, S. T. Brown, and B. H. Lambrigsten, "Analysis of array distortion in a microwave interferometric radiometer: Application to the GeoSTAR project," *IEEE Trans. Geosci. Remote Sens.*, vol. 45, no. 7, pp. 1958–1966, Jul. 2007.

[6] D. H. Staelin and C. Surussavadee, "Precipitation retrieval accuracies for geo-microwave sounders," *IEEE Trans. Geosci. Remote Sens.*, vol. 45, no. 10, pp. 3150–3159, Oct. 2007.

[7] J. Christensen, A. Carlstrom, H. Ekstrom, P. de Maagt, A. Colliander, A. Emrich, and J. Embretsen, "GAS: The Geostationary Atmospheric Sounder," in *Proc. IEEE IGARSS*, 2007, pp. 223–226.

[8] W. Ji, Z. Cheng, L. Hao, S. Weiying, and Y. Jingye, "Clock scan of imaging interferometric radiometer and its applications," in *Proc. IEEE IGARSS*, Barcelona, Spain, 2007, pp. 5244–5246.

[9] M. A. Janssen, *Atmospheric Remote Sensing by Microwave Radiometry*. New York: Wiley, 1993.

[10] B. A. Burns, X. Wu, and G. R. Diak, "Effects of precipitation and cloud ice on brightness temperatures in AMSU moisture channels," *IEEE Trans. Geosci. Remote Sens.*, vol. 35, no. 6, pp. 1429–1437, Nov. 1997.

[11] F. Karbou, É. Gérard, and F. Rabier, "Microwave land emissivity and skin temperature for AMSU-A and -B assimilation over land," *Q. J. R. Meteorol. Soc.*, vol. 132, no. 620, pp. 2333–2355, 2006.

[12] F. Karbou, C. Prigent, L. Eymard, and J. R. Pardo, "Microwave land emissivity calculations using AMSU measurements," *IEEE Trans. Geosci. Remote Sens.*, vol. 43, no. 5, pp. 948–959, May 2005.

[13] J. I. Antonov, R. A. Locarnini, T. P. Boyer, A. V. Mishonov, and H. E. Garcia, *World Ocean Atlas 2005*, vol. 2, *Salinity*, S. Levitus, Ed. Washington, DC: U.S. Gov. Printing Office, 2006.

[14] P. Minnis, L. Nguyen, D. R. Doelling, D. F. Young, W. F. Miller, and D. P. Kratz, "Rapid calibration of operational and research meteorological satellite imagers. Part I: Evaluation of research satellite visible channels as references," *J. Atmos. Ocean. Technol.*, vol. 19, no. 9, pp. 1233–1249, 2002.

[15] P. Rabindra, P. Minnis, D. A. Spangenberg, M. M. Khaiyer, M. L. Nordeen, J. K. Ayers, L. Nguyen, Y. Yi, P. K. Chan, Q. Z. Trepte, F. L. Chang, and W. L. Smith, Jr., "NASA-Langley web-based operational real-time cloud retrieval products from geostationary satellites," *Proc. SPIE*, vol. 6408, p. 640 81P, 2006.

[16] "Land/sea/lake definition," GODAE High Resolution Sea Surface Temperature Pilot Project, 2002.

[17] "2-minute gridded global relief data (ETOPO2v2)," U.S. Dept. Commerce, Nat. Ocean. Atmos. Admin., Nat. Geophys. Data Center, Boulder, CO, 2006.

[18] L. Klein and C. Swift, "An improved model for the dielectric constant of sea water at microwave frequencies," *IEEE Trans. Antennas Propag.*, vol. AP-25, no. 1, pp. 104–111, Jan. 1977.

[19] G. Deblonde and S. English, "Evaluation of the FASTEM2 fast microwave oceanic surface emissivity model," in *Proc. Int. ATOVS Study Conf.*, Budapest, Hungary, 2000.

[20] P. Rosenkranz, "Water vapor microwave continuum absorption: A comparison of measurements and models," *Radio Sci.*, vol. 33, no. 4, pp. 919–928, 1998.

[21] D. Staelin, "Measurements and interpretation of the microwave spectrum of the terrestrial atmosphere near 1-centimeter wavelength," *J. Geophys. Res.*, vol. 71, pp. 2875–2881, Jun. 1966.

[22] E. M. Feæigel§son, *Light and Heat Radiation in Stratus Clouds: Radiatsionnye Protsessy v Sloistoobraznykh Oblakakh*. Jerusalem: Israel Program Sci. Transl., 1966.

[23] J. P. Snyder, *Map Projections: A Working Manual*. Washington, DC: U.S. Gov. Printing Office, 1987.

[24] J. C. Ehrhardt, "Hexagonal fast Fourier transform with rectangular output," *IEEE Trans. Signal Process.*, vol. 41, no. 3, pp. 1469–1472, Mar. 1993.

[25] A. Camps, J. Bara, I. C. Sanahuja, and F. Torres, "The processing of hexagonally sampled signals with standard rectangular techniques: Application to 2-D large aperture synthesis interferometric radiometers," *IEEE Trans. Geosci. Remote Sens.*, vol. 35, no. 1, pp. 183–190, Jan. 1997.

[26] A. Thompson and L. D'Addario, "Frequency response of a synthesis array: Performance limitations and design tolerances," *Radio Sci.*, vol. 17, no. 2, pp. 357–369, Mar./Apr. 1982.

[27] A. B. Tanner, B. H. Lambrigtsen, and T. C. Gaier, "A dual-gain antenna option for GeoSTAR," in *Proc. IEEE IGARSS*, Barcelona, Spain, 2007, pp. 227–230.

[28] F. T. Ulaby, R. K. Moore, and A. K. Fung, *Microwave Remote Sensing: Active and Passive*. Reading, MA: Addison-Wesley, 1981.

[29] Y. H. Kerr, P. Waldteufel, J. P. Wigneron, and J. Font, "The Soil Moisture and Ocean Salinity mission: The science objectives of an L band 2-D interferometer," in *Proc. IEEE IGARSS*, Honolulu, HI, 2000, pp. 2969–2971.

[30] E. Anterrieu, P. Waldteufel, and A. Lannes, "Apodization functions for 2-D hexagonally sampled synthetic aperture imaging radiometers," *IEEE Trans. Geosci. Remote Sens.*, vol. 40, no. 12, pp. 2531–2542, Dec. 2002.

[31] A. B. Tanner and C. T. Swift, "Calibration of a synthetic aperture radiometer," *IEEE Trans. Geosci. Remote Sens.*, vol. 31, no. 1, pp. 257–267, Jan. 1993.

[32] J. A. Högbom, "Aperture synthesis with a non-regular distribution of interferometer baselines," *Astron. Astrophys., Suppl.*, vol. 15, pp. 417–426, Jun. 1974.

[33] A. Camps, "Extension of the clean technique to the microwave imaging of continuous thermal sources by means of aperture synthesis radiometers—Abstract," *J. Electromagn. Waves Appl.*, vol. 12, no. 3, pp. 311–313, 1998.



Boon H. Lim (S'06–M'09) received the B.S. and M.S. degrees in electrical engineering and the Ph.D. degree in geoscience and remote sensing from the University of Michigan, Ann Arbor (UMich), in 1999, 2001, and 2008, respectively.

He was a Staff Engineer with the Space Physics Research Laboratory, Department of Atmospheric, Oceanic and Space Sciences, College of Engineering, UMich, from 2002 to 2003. He was a Graduate Student Research Assistant with the Remote Sensing Group, Department of Atmospheric, Oceanic and Space Sciences, College of Engineering, UMich, from 2004 to 2008, where his research involved microwave remote-sensing calibration and instrumentation, including synthetic aperture radiometry. He is currently a member of the Microwave Systems Technology Group, Jet Propulsion Laboratory, Pasadena, CA.

Dr. Lim was a recipient of the NASA Earth System Science Fellowship from 2005 to 2008 to work on the "Development of a Geosynchronous Temperature and Humidity Sounder/Imager" and of the NASA Group Achievement Award as a member of the Lightweight Rainfall Radiometer Instrument Team.



Christopher S. Ruf (S'85–M'87–SM'92–F'01) received the B.A. degree in physics from Reed College, Portland, OR, and the Ph.D. degree in electrical and computer engineering from the University of Massachusetts, Amherst.

He is currently a Professor of atmospheric, oceanic, and space sciences and electrical engineering and computer science and the Director of the Space Physics Research Laboratory, Department of Atmospheric, Oceanic and Space Sciences, College of Engineering, University of Michigan, Ann Arbor. He was previously with Intel Corporation, Hughes Space and Communication, the NASA Jet Propulsion Laboratory, Pasadena, CA, and Penn State University, University Park. In 2000, he was a Guest Professor with the Technical University of Denmark, Lyngby, Denmark. He has published in the areas of microwave-radiometer satellite calibration, sensor and technology development, and atmospheric, oceanic, land-surface, and cryosphere geophysical retrieval algorithms.

Dr. Ruf is a member of the American Geophysical Union (AGU), the American Meteorological Society (AMS), and Commission F of the Union Radio-Scientifique Internationale. He has served on the editorial boards of the AGU *Radio Science*, the IEEE TRANSACTIONS ON GEOSCIENCE AND REMOTE SENSING (TGRS), and the AMS *Journal of Atmospheric* and *Oceanic Technology*. He is currently the Editor-in-Chief of TGRS. He was a recipient of three NASA Certificates of Recognition and four NASA Group Achievement Awards, as well as the 1997 TGRS Prize Paper Award, the1999 IEEE Resnik Technical Field Award, and the IGARSS 2006 Symposium Prize Paper Award.

Authorized licensed use limited to: University of Michigan Library. Downloaded on October 30, 2009 at 15:29 from IEEE Xplore. Restrictions apply.